Lab on a Chip

PAPER

View Article Online
View Journal | View Issue

Cite this: *Lab Chip*, 2015, **15**, 216

Magnetofluidic platform for multidimensional magnetic and optical barcoding of droplets†

Gungun Lin,*[ab] Denys Makarov,[a] Mariana Medina-Sánchez,[a] Maria Guix,[a] Larysa Baraban,[c] Gianaurelio Cuniberti[cd] and Oliver G. Schmidt[ab]

Received 1st October 2014,
Accepted 7th October 2014

DOI: 10.1039/c4lc01160k

www.rsc.org/loc

We present a concept of multidimensional magnetic and optical barcoding of droplets based on a magnetofluidic platform. The platform comprises multiple functional areas, such as an encoding area, an encoded droplet pool and a magnetic decoding area with integrated giant magnetoresistive (GMR) sensors. To prove this concept, penicillin functionalized with fluorescent dyes is coencapsulated with magnetic nanoparticles into droplets. While fluorescent dyes are used as conventional optical barcodes which are decoded with an optical decoding setup, an additional dimensionality of barcodes is created by using magnetic nanoparticles as magnetic barcodes for individual droplets and integrated micro-patterned GMR sensors as the corresponding magnetic decoding devices. The strategy of incorporating a magnetic encoding scheme provides a dynamic range of ~40 dB in addition to that of the optical method. When combined with magnetic barcodes, the encoding capacity can be increased by more than 1 order of magnitude compared with using only optical barcodes, that is, the magnetic platform provides more than 10 unique magnetic codes in addition to each optical barcode. Besides being a unique magnetic functional element for droplet microfluidics, the platform is capable of on-demand facile magnetic encoding and real-time decoding of droplets which paves the way for the development of novel non-optical encoding schemes for highly multiplexed droplet-based biological assays.

Introduction

The recent development of droplet-based microfluidic technologies has provoked revolutionary changes in the standard methodology of performing microbiological and bioanalytical assays.[1–3] Prominent examples among many successful studies are DNA sequencing,[4] droplet-based polymerase chain reaction (PCR),[5] and drug resistance tests,[6] just to point out a few. This new approach is advancing in fundamental science as an effective tool for studying *in vivo* and *in vitro* directed evolution[7] and cell biology.[8] Droplet microfluidics allows the compartmentalization of biochemical species in volumes ranging from picoliters to a few nanoliters,[9] which has boosted the performance of various clinical and analytical assays to a new level in terms of precision and time efficiency.[10]

As an alternative to conventional microplates which are position-indexed, highly multiplexed droplet-based biological assays benefit from the assignation of unique codes to individual droplets (small microreactors) so that different compounds or variants can be screened or identified from a large library.[11] For instance, drug discovery may require screening of as many as ~10^6 variants from small compound libraries, which accordingly requires an equal number of barcodes to be created.[12] A variety of optical codes, *e.g.*, spectroscopic or graphical barcodes based on discrete metallic layers,[13] photonic crystals,[14,15] fluorescent molecules[16,17] or quantum dots,[18,19] are available. Although most of these optical codes were prepared *off-chip* primarily for applications in suspension arrays, they can be potentially used in droplet microfluidics. In this case, each unique code can be associated with a corresponding compound or variant prior to encapsulation into droplets.[11] However, they present limitations regarding their applications, *i.e.*, in drug development, where the preparation of a large number of different concentrations of drugs for screening would be highly laborious, time consuming and costly. An alternative solution is to directly prepare barcodes *on-chip* by droplet microfluidics, which has been proven as a facile approach that allows for precise control over the size, shape and composition of synthesized particles.[20–22] Recently, a droplet barcode generator

[a] *Institute for Integrative Nanosciences, IFW Dresden, Helmholtzstr. 20, 01069 Dresden, Germany. E-mail: g.lin@ifw-dresden.de*
[b] *Material Systems for Nanoelectronics, Chemnitz University of Technology, Reichenhainerstr. 70, 09107 Chemnitz, Germany*
[c] *Max Bergmann Center of Biomaterials, Dresden University of Technology, Budapesterstr. 27, 01069 Dresden, Germany*
[d] *Division of IT Convergence Engineering, POSTECH, Pohang, Korea*
† Electronic supplementary information (ESI) available. See DOI: 10.1039/c4lc01160k

has been demonstrated to be capable of generating barcodes based on concentration gradients of two-color fluorescent dyes, alleviating the need for *off-chip* encoding prior to droplet encapsulation.[23]

The combination of two or more color codes with increasing dimensionalities to extend the encoding capacity has become an emerging trend as the number of unique codes is determined by[24] $C = N^m - 1$, where N is the intensity level and m is the dimensionality of barcodes, or in other words, the number of color codes combined. Nonetheless, the total number of barcodes that can be put into real practice is restricted by several issues, such as the limited dynamic range of an optical decoding setup[11] or spectral overlap,[19] which accordingly limit the values of N and m. For instance, commercial Luminex® beads can produce about 100 codes using two fluorescent dyes,[25] which is by far not sufficient to address the needs of large screens such as the identification of ~1 million variants.[12] Although the capacity can be increased by adding more colors, it requires more fluorescence detectors to be included, which makes the measurement rather bulky and expensive. The spectrometer can be used to resolve multiple wavelengths simultaneously, but the decoding process is slow and the throughput is limited. Therefore, it is highly desired to further expand the dynamic range and the library of existing codes, which can be achieved by relying on complementary non-optical codes. Further, some complex biological assays may be vulnerable to light due to absorption or autofluorescence of the sample matrix and thus these would greatly benefit from the development of a non-optical encoding method.

The interaction of magnetism and microfluidics has given birth to the emerging field of micro-magnetofluidics.[43] Particularly, magnetic particles have become an attractive alternative to conventional optical markers in a variety of applications,[26] *e.g.*, for point-of-care diagnostics,[27] immunological assays[28,29] and flow cytometry.[30,31] As most biological samples are free from any magnetic background, the detection of magnetically labeled entities[32–37] with magnetic sensors is more suited for analyses of complex samples than optical markers. In droplet microfluidics, magnetic particles are encapsulated in droplets for the detection,[44] actuation,[45] and on-chip manipulation of liquids[46] or cargos[47] by coupling with external magnetic fields. Magnetic particles have also been used for the synthesis of barcodes. For instance, magnetic graphical barcodes based on hydrogel microparticles were synthesized in microfluidics.[48] However, the throughput is limited by the decoding process as it relies on visual inspection which is slow and not suitable for droplet microfluidics. Multifunctional optical barcodes combining magnetic particles have been created in droplet microfluidics with an additional functionality such as barcode manipulation.[20,22] So far, there is no magnetofluidic platform which is capable of on-demand facile generation of magnetic droplet barcodes and performs high-throughput real-time decoding of emulsion droplets. In addition, the adoption of magnetic particles to add an additional dimensionality to conventional optical codes in order to expand the encoding capacity that can be accordingly decoded remains elusive.

Here, we present the concept of magnetic encoding of emulsion droplets and its extension as hybrid magnetic–optical barcodes for droplet-based microfluidics. Magnetic nanoparticles and GMR sensors are introduced as non-optical barcodes and decoding devices, respectively. To prove this concept, we established a droplet-based magnetofluidic platform comprising a series of lab-on-a-chip functional areas including an encoding area, an encoded droplet pool for storage, and a magnetic decoding area, representing the first strategy to perform magnetic–optical joint barcoding and decoding of emulsion droplets (Fig. 1). Penicillin was chosen as a drug model for the proof-of-concept demonstration due to its relevance to the treatment of bacterial infections[38] and the study of drug-binding mechanisms.[39] Droplet barcodes of bivariates combining both magnetic voltage signals and fluorescence signals can be easily generated in full-range combinations. The introduction of magnetic nanoparticles into the family of droplet barcodes adds an additional dimensionality to conventional optical barcodes which increases the encoding capacity by more than 1 order of magnitude, that is, more than 10 magnetic barcodes can be additionally provided for each optical barcode.

Materials and methods

Fabrication and characterization of GMR sensors

The volume of emulsion droplets generally ranges from picoliters to a few nanoliters in droplet microfluidics.[9] Droplets containing small amounts of magnetic nanoparticles impose stringent requirements on the sensitivity of GMR sensors. To detect such small entities of magnetic materials, the size of the sensing element must be compatible to the size of the objects of interest in order to ensure the highest sensitivity. We chose a highly sensitive GMR sensor as a magnetic decoding element which is composed of $[\mathrm{Py}\ (1.5\ \mathrm{nm})/\mathrm{Cu}\ (2.3\ \mathrm{nm})]_{30}$ ($\mathrm{Py} = \mathrm{Ni_{81}Fe_{19}}$) coupled at the 2nd antiferromagnetic maximum. The GMR sensors were structured into a meander which is composed of 19 turns of $3 \times 100\ \mu\mathrm{m}^2$ GMR stripes, covering a total sensing area of approximately $100 \times 100\ \mu\mathrm{m}^2$ (Fig. 2b-1). This design allows the sensitive detection of magnetic stray fields over an enlarged area of droplets, which is suitable for the purpose of quantification.

To prepare the GMR sensors, a thermally oxidized silicon substrate with 600 nm oxide was patterned using a standard photolithography technique (see details in the ESI†). Firstly, the AZ5214E photoresist (MicroChem, AZ5214E) was spin-coated on the substrate with a spin speed of 4500 rpm. Then it was exposed with a mask aligner (MJB4, Karl Suss) by using a photo mask coated with patterned meandered chromium, leading to a final pattern with a meandered shape with 19 turns of stripes. Each of them has a dimension of $3 \times 100\ \mu\mathrm{m}^2$. Afterwards, the substrate was baked at 120 °C

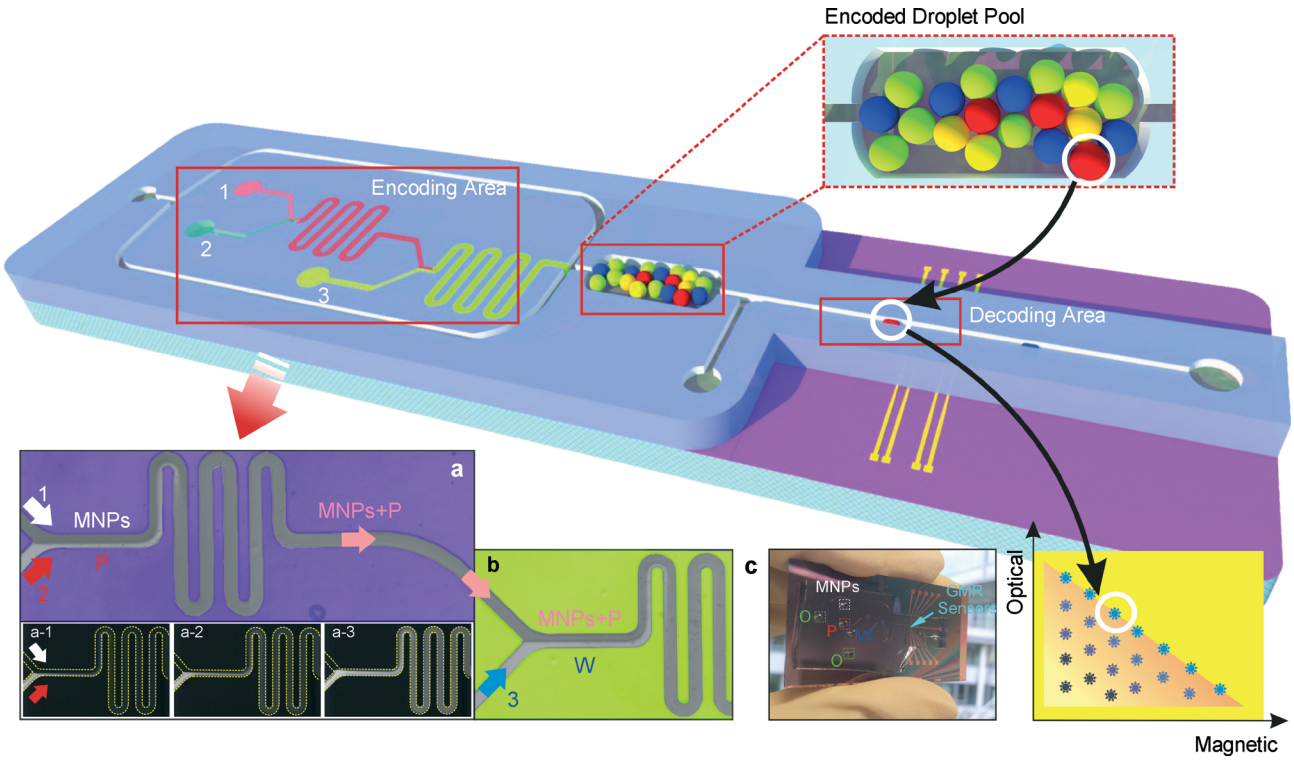

Fig. 1 Conceptual image of a lab-on-a-chip droplet-based magnetofluidic platform which is composed of several functional areas (marked by squares): (1) an encoding area, (2) an encoded droplet pool for storage, and (3) a decoding area. (a) A colour-coded micrograph of the coencapsulation area for magnetic nanoparticles (MNPs) and fluorescent penicillin (P). (b) Water (W) is used to dilute the mixture of MNPs and P. Arrows indicate the flow direction. Fluorescence micrographs of the coencapsulation of MNPs and P using different combinations of flow parameters: MNPs: 8 nl s^{-1}, P: 2 nl s^{-1} (a-1); MNPs: 5 nl s^{-1}, P: 5 nl s^{-1} (a-2); and MNPs: 2 nl s^{-1}, P: 8 nl s^{-1} (a-3). (c) An optical photograph of the magnetofluidic platform with integrated GMR sensors. Dashed squares indicate the inlets where magnetic nanoparticles (MNPs), oils (O), penicillin (P) and water (W) are injected. (Bottom right) A schematic diagram of two-dimensional barcodes based on joint optical and magnetic voltage signals produced by combining the coencapsulation of MNPs, penicillin and water. Each point inside the diagram represents a single joint droplet barcode.

for 2 min followed by flood exposure for 30 s. Finally, the substrate coated with the photoresist was dipped in a developer (MIF726, MicroChem) for 1 min, rinsed with DI water and dried with compressed air. GMR sensors were deposited on the lithographically-patterned silicon substrate by magnetron sputtering. Before deposition, a base pressure of around 5.4×10^{-7} mbar was reached. During deposition, Ar was used to generate the plasma, the flow rate of which was maintained at 10 sccm and the pressure was 9.4×10^{-4} mbar. After fabrication of the GMR sensors, a second lithography step was performed to pattern electrical contacts which are precisely aligned with the sensors. We used Ta (5 nm)/Cu (200 nm)/Ta (5 nm) as the conducting materials.

Magnetoelectrical characterization of the integrated GMR sensor is shown in Fig. 2d. The sensor shows a GMR ratio of 11%. The GMR ratio is defined as the relative change of sample resistance with magnetic field H_{ext}:[40] $GMR(H_{ext}) = (R(H_{ext}) - R(H_{sat}))/R(H_{sat})$, where $R(H_{sat})$ is the sensor resistance when a saturating magnetic field, H_{sat}, is applied. In this case, a magnetic field of 300 Oe is sufficient to saturate the sensor. The channel has a width of 100 μm and a height of 80 μm. The sensor presents a maximum sensitivity of 0.3% Oe^{-1} at a low field of 10 Oe, which ensures the successful detection of magnetic objects on-chip. Here the sensitivity is given by[40] $S(H_{ext}) = [dR(H_{ext})/dH_{ext}]/R(H_{sat})$.

Integration of the GMR sensors in the microfluidic device

For the related microfluidic applications, electrical insulation of the sensors is required so as to avoid current shunting and leakage. We spin-coated a layer of SU-8 2 (MicroChem) on top of the GMR sensors with a spin speed of 8000 rpm, resulting in a thickness of the insulation layer of about 700 nm. The encapsulation layer of SU-8 2 was baked at 90 °C for 5 min and exposed to UV by using the mask aligner (Karl Suss, MJB4) for 30 s.

The microfluidic channel was fabricated by soft lithography. Firstly, a channel mold was fabricated on a silicon wafer by using SU-8 50 with a spin speed of 1200 rpm leading to a channel thickness of about 80 μm. The geometry of the mold was created by using a direct microwriter (MicroWriter Baby, Durham Magneto Optics Ltd.) to expose selective areas of the photoresist SU-8 50. The unexposed areas were removed by using the developer (mr-Dev 600, micro resist technology GmbH). Afterwards, a polydimethylsiloxane

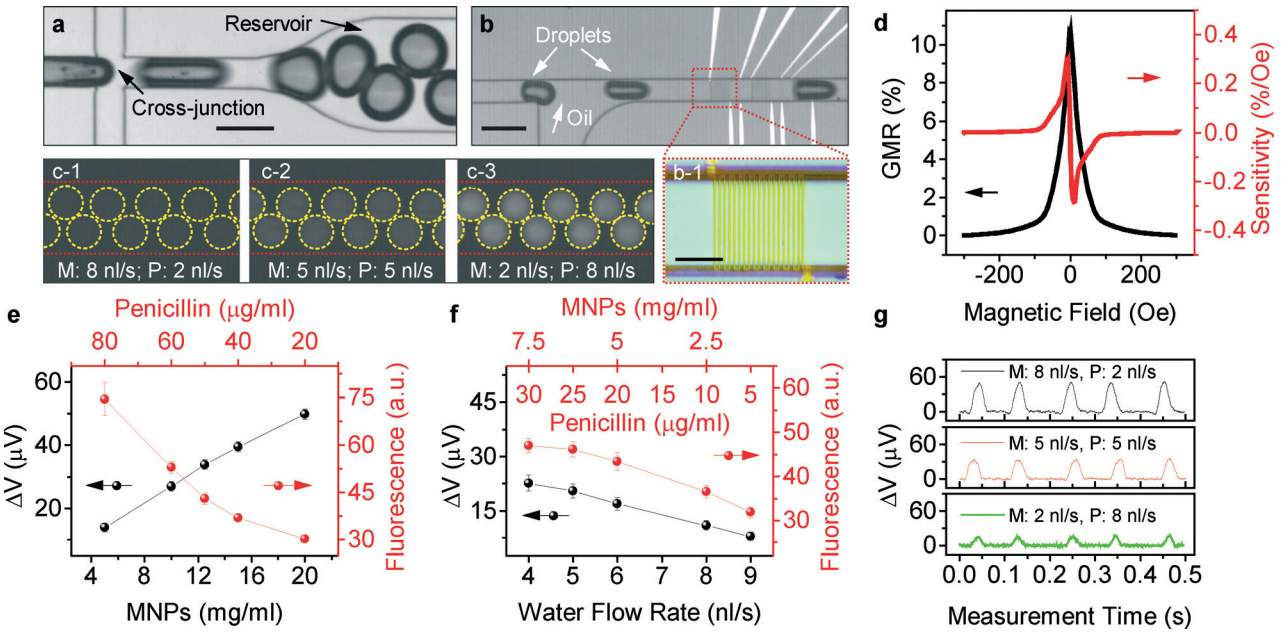

Fig. 2 (a) Bright-field micrograph of a cross-junction for droplet formation and a reservoir (droplet pool). (b) A bright-field micrograph of droplet reinjection and detection by GMR sensors. (b-1) An optical micrograph of a GMR sensor with a meander shape integrated in the microfluidic channel. Scale bars in (a) and (b): 200 μm, in (b-1): 50 μm. (c1–c3) Evolution of the fluorescence contrast of the emulsion droplets in the droplet pool with the change of flow rates of magnetic nanoparticles (M) and fluorescent penicillin (P). Red dashed lines indicate the edge of the microfluidic channel. Yellow dashed circles indicate the location of the emulsion droplets. The size of the droplets is 150 μm in diameter. (d) Magnetoelectrical characterization of an integrated GMR sensor. (e) Comparison of the measured fluorescence intensity (red) and the measured voltage amplitude (black) of the detection peaks of the emulsion droplets using a GMR sensor during the coencapsulation of magnetic nanoparticles (MNPs) and penicillin *via* the two injection channels 1 and 2. (f) Comparison of the measured fluorescence intensity (red) and the measured voltage amplitude (black) when the flow rate of water is increased in channel 3 while the flow rate of MNPs and penicillin is kept constant. The lines are guides to the eyes. (g) Real-time detection of emulsion droplets using a GMR sensor which are produced at different flow rates of magnetic nanoparticles (M) and fluorescent penicillin (P) with the flow rate of water being 0.

(PDMS) prepolymer (Sylgard 184, Dow Corning) was prepared by mixing the polymer with a cross-linking agent in a ratio of 1 : 10 wt.%, after which it was degassed for 30 min. The mixture was poured into the mold and cured at 180 °C for 10 min. The cured PDMS channel was peeled off the mold, and the corresponding inlets and outlets were created by using a biopsy puncher with a diameter of 1 mm.

The assembly of PDMS with the bottom substrate was performed by means of amine–epoxy chemistry.[41] Firstly, the PDMS channel was activated by N_2 plasma with a power of 40 mW for 30 s creating amine groups on its surface. Then it was brought into contact with the silicon chip with integrated GMR sensors. After careful alignment of the sensor with the channel under a microscope, the device was baked at 120 °C for 30 min to achieve permanent bonding. A photograph of the final assembled magnetofluidic device is shown in Fig. 1c.

Sensor characterization and real-time measurements

The characterizations of GMR sensors were performed by using a magnetoelectrical measurement setup. The sensor was placed in a sample holder for a standard 4-probe resistance measurement. For magnetoelectrical characterizations, the sensor was placed in the pole shoes of electromagnets where uniform magnetic fields are applied. The corresponding resistance change of the sensor was simultaneously recorded with a computer-controlled multimeter (Keithley 2000). The magnetic field was cycled between ±300 Oe, which is sufficient to measure a full-range response of the GMR sensor.

For the detection of droplets, the sensor was included as a component of a Wheatstone bridge, providing differential voltage. The signal from the bridge was fed into a lock-in amplifier (SRS 830), which was used to reduce the noise and amplify the signal. The output of the lock-in amplifier was picked up by a data acquisition box (NI USB 6009) at a sampling rate of 5 kHz. An internal sinusoidal ac signal with a frequency of 1 kHz was used as a reference. The measuring current was set at 1 mA. An external permanent magnet (A1045, IBS Magnet) was placed under the sensor. The position of the magnet was adjusted carefully *via* monitoring the signal output in order to bias the sensor to the most sensitive region. The magnetic field of the permanent magnet was used not only for sensing purposes but also to simultaneously magnetize the superparamagnetic nanoparticles.

Droplet barcoding

For on-chip droplet production, mineral oil (Sigma Aldrich, M8510) with 5% SPAN 80 was used as the continuous phase,

and ferrofluid nanoparticles (chemicell, fluidMAG-PAS, the corresponding data sheet in the ESI†) either diluted with deionized water or coencapsulated with fluorescent penicillin (BOCILLIN FL, Life Technologies) were used as the dispersed phase. The penicillin was functionalized with a BODIPY fluorescent dye which emits green fluorescence at 510 ± 4 nm. Penicillin is still active against microbes as it has been extensively used to identify penicillin-binding proteins.[54–56]

To perform barcoding, fluids filled in separate syringes were pumped into the device by external syringe pumps (Cetoni GmbH). For the demonstration of droplet barcoding, the device was operated in a *squeezing* regime to produce droplets of defined volumes for subsequent intensity encoding. In the *squeezing* regime, the volume of droplets is determined solely by the ratio of the flow rates of the continuous phase and the dispersed phase,[49] characterized by a relatively low capillary number with a low flow speed. In the present study, the flow rate of oil was kept constant at 30 nl s^{-1}, and the flow rate of the dispersed phase (including magnetic nanoparticles and penicillin) was kept constant at 10 nl s^{-1} to ensure that the ratio of the flow rates of the continuous and the dispersed phase was the same. To vary the concentration of each component in the droplets, only the ratio of the flow rate of each component was changed.

Results and discussion

A magnetofluidic platform for droplet barcoding

The platform comprises multiple functional areas to perform multiple tasks (Fig. 1). We designed an encoding area (Fig. 1a and b) where different species of biological interest (*e.g.* drugs, proteins, DNAs) can be encoded with magnetic nanoparticles (MNPs) or fluorescent dyes by being coencapsulated into the microfluidic channel. In our particular case, our study will be focused on penicillin which was previously functionalized with a BODIPY fluorescent dye.

The encoding area consists of a main channel flanked by several side channels. In our work, MNPs were injected from the top channel (channel 1, in Fig. 1a) and penicillin was injected from the bottom channel (channel 2, in Fig. 1a) in a laminar flow. After the junction, a serpentine channel serves as a flow damper, facilitating lateral mixing of penicillin and MNPs by diffusion. The coencapsulation process represents the first step to bring the magnetic or optical codes into droplets together with other biochemical species to be encoded, *i.e.* penicillin. The same principle could also be extended in case more channels are added (channel 3 in Fig. 1b) to encode more species within the droplets.

The evolution of the two fluids (fluorescent penicillin and magnetic nanoparticles) in the coencapsulation area with respect to the variation of the flow rates is displayed in Fig. 1a1–a3. Firstly, we kept the flow rate of water in the dilution channel at 0. By competing injection of two fluids with different flow rates, the concentrations of the encapsulated biochemical components can be varied in the subsequently produced droplets.

Droplets formed at a cross-junction are afterwards directed into an enlarged dimension of the microfluidic channel (Fig. 2a, reservoir), facilitating optical observation that alleviates the need for increasing the frame rates of a high-speed camera that may reduce the optical intensity. Right behind the reservoir, the droplets are further reinjected into the microfluidic channel for decoding (Fig. 2b). In this case, oil is injected from a side channel to increase the spacing to avoid potential interference during magnetic measurements. GMR sensors served as the decoding devices for the encoded droplets.

The encoded droplets are decoded both by magnetic and optical means. Fig. 2c1–c3 compare several groups of emulsion droplets with different concentrations of coencapsulated MNPs and penicillin employing only the two injection channels 1 and 2 (see Fig. 1). The location of the droplets is indicated by dashed circles. The detection of these droplets with a GMR sensor is shown in Fig. 2g. Each isolated peak represents the detection of a single emulsion droplet. The amplitude of the detection peaks obtained by the GMR sensor and the fluorescence intensity of the corresponding droplets are further compared in Fig. 2e. As the magnetic voltage signal reflects the amount of MNPs inside the droplets and the fluorescence signal is related to the concentration of penicillin inside the droplets, the inverse dependency of the fluorescence intensity and the magnetic signals evidences the competing injection process of MNPs and fluorescent penicillin during the coencapsulation process. To encode droplets encapsulating only one biochemical species of a single variant, *i.e.*, penicillin with variation in the concentration, it is sufficient to use only two injection channels with either different concentrations of MNPs or fluorescent dyes as barcodes. The advantage of coencapsulating MNPs with fluorescent dyes is that when penicillin is diluted to the low concentration range, the weak intensity of the fluorescence signal is challenging to detect. The coencapsulation of higher concentrations of MNPs can easily provide an additional dynamic range of ~40 dB without the need to worry about sensor saturation (Fig. S2, ESI†).

Joint magnetic and optical barcoding of droplets

To encode droplets carrying more biochemical species for combinatorial analysis, additional injection channels should be included. Thus, barcodes of bi- or multi-variants could be used to encode droplets carrying more species. In this case, we used water as a buffer to create two-dimensional barcodes based on joint fluorescence and magnetic voltage signals. The real-time magnetic detection of these encoded droplets is shown in Fig. S1, ESI.† The coencapsulation of water dilutes the mixture of MNPs and penicillin by increasing the rate of water (Fig. 2f). It is worth noting that opaque MNPs can block part of the emission from fluorescent dyes which is evidenced by the decrease in the fluorescence intensity with an increase in the concentration of MNPs (Fig. S3†). It accounts for the deviation of the dependency of the fluorescence intensity from a linear relationship

at higher concentrations of magnetic nanoparticles (Fig. 2e and f). The deviation from a linear behavior at the low fluorescence intensity range in Fig. 2e could be partially ascribed to the fact that the low fluorescence intensity falls out of the linear detection range of the optical detector. Considering the fact that magnetic nanoparticles may block part of the fluorescence emission, further increasing the total number of multidimensional hybrid magnetic and optical barcodes can be performed using highly magnetized low concentration magnetic nanoparticles[57] in order to alleviate the issue.

We used an encoding diagram to summarize the joint fluorescent and magnetic barcodes (Fig. 3a). For a single coencapsulation process of MNPs and fluorescent penicillin using two injection channels (channels 1 and 2 in Fig. 1a), fluorescent penicillin is diluted by a solution of MNPs. Different concentrations of penicillin can be associated with either the fluorescence signal or the magnetic signal. The barcodes are located along the blue line as indicated in the diagram. Due to the completing injection mechanism, a higher concentration of penicillin is associated with lower magnetic voltage signals. When another channel (channel 3 in Fig. 1b) was used to inject additional chemicals, both fluorescence and magnetic voltage signals were used as joint barcodes; thus, the diagram of the barcodes is expanded in the direction as indicated by the arrow, which spans a triangular area enclosed by the two background lines (dashed lines) and the coencapsulation line (blue solid line). With appropriate and selective concentrations and flow rates of fluorescent dyes, MNPs and the buffer (water), a full range of droplet barcodes covering the whole triangular area can be produced on demand.

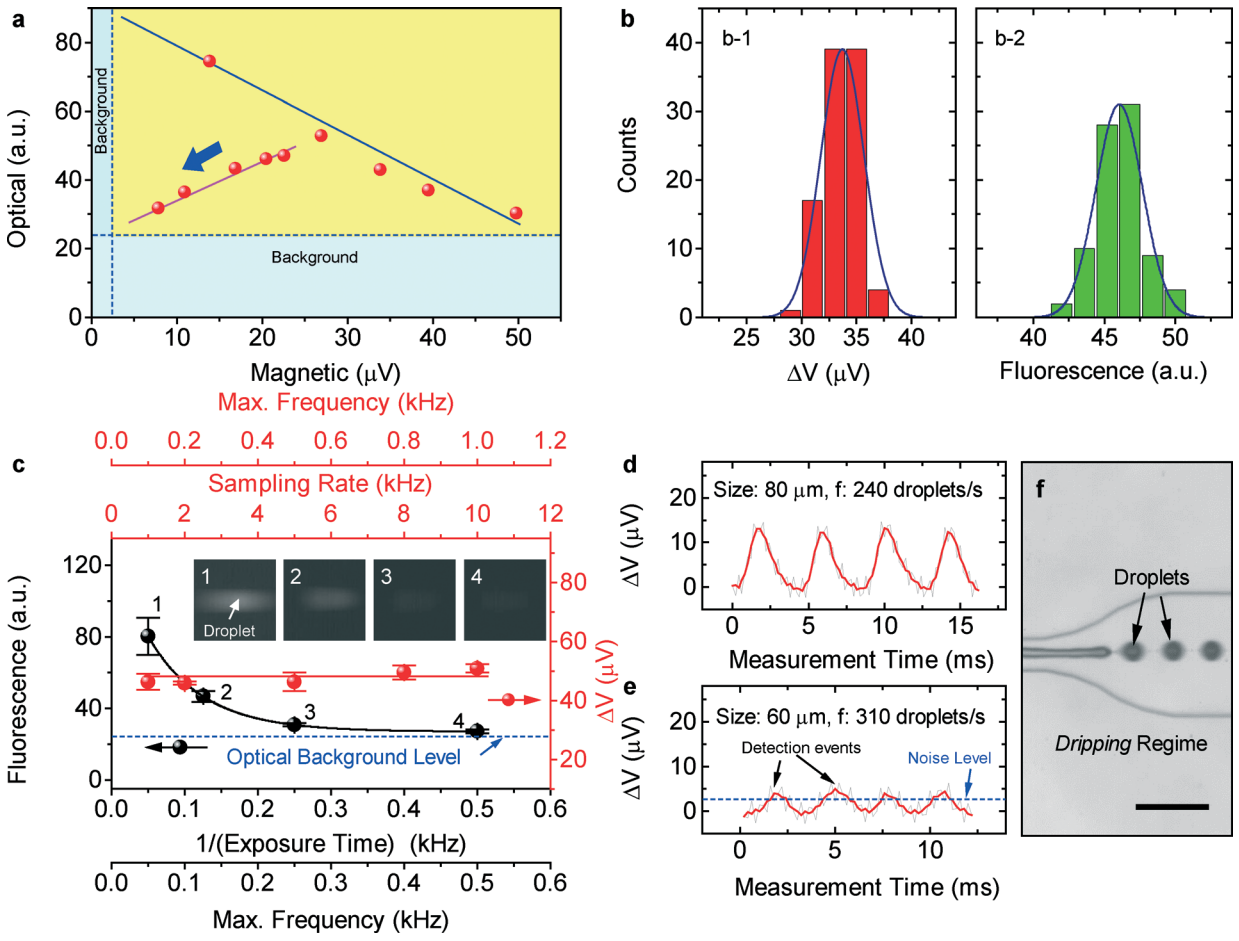

Fig. 3 (a) Two-dimensional barcoding phase diagram based on joint optical and magnetic signals. The dashed lines are the corresponding background levels of fluorescence and magnetic measurements. The solid lines are guides to the eyes. (b) Histograms of the measured magnetic voltage signal amplitudes (b-1) and fluorescence intensity (b-2) over about 100 droplets produced under selective flow parameters: MNPs: 5 nl s^{-1}, fluorescent penicillin: 5 nl s^{-1}. The curves are Gaussian fits to the histograms. (c) Comparison of the dependence of magnetic voltage signals (red) and fluorescence signals (black) on the sampling rate of a data acquisition box (DAQ) and the frame rate (equal to $1/t$, where t is the exposure time) of a high-speed camera, respectively. *Max. frequency* is the maximum measurable droplet frequency with respect to the corresponding settings of the sampling (frame) rate of the DAQ or optical detectors. Insets 1 to 4 are fluorescence graphs of a droplet taken at different frame rates (50, 125, 250 and 500 fps) of the high-speed camera. Real-time detection of the emulsion droplets was conducted at a frequency of ~240 droplets per second (d) and ~310 droplets per second (e). The red lines are curves smoothed by 2-point adjacent averaging. The droplets are produced at a high frequency by dripping into the immiscible oil (f). Scale bar: 200 μm.

The sensitivity of the system for producing distinguishable droplet barcodes can be evaluated from the standard deviation (σ) of fluorescence/magnetic signals measured over a large array of as-produced droplets under selective flow parameters. The analysis of histograms of decoded signals (Fig. 3b) reveals that the standard deviations of magnetic voltage signals and fluorescence intensity measured over a large array of as-produced droplets under selective flow parameters are ~1.5 μV and ~1.6, respectively. About 96% of droplets can be reproduced within a confidence interval (2σ). Thus, with an initial concentration of fluorescent penicillin (100 μg ml^{-1}, fluorescence intensity: ~100) and a supplied concentration (25 mg ml^{-1}, magnetic voltage signal: ~60 μV) of magnetic nanoparticles (chemicell, fluidMAG) used for the experiments, an approximation of about 200 joint two-dimensional distinguishable codes (optical: $k \approx 20$, magnetic: $l \approx 20$, $C = (k \times l)/2$) can be produced. The number could be scaled up by using highly magnetized magnetic nanoparticles. In addition, the microfluidic flow conditions and the sensitivity of the device could be improved to minimize the standard deviations so that the number of distinguishable codes can be increased.

The facile approach of introducing MNPs into the family of droplet encoding schemes is more advantageous than using solely optical codes and can be used as an alternative approach in some applications especially when droplets are formed or reinjected into the microfluidic channel at a frequency as high as ~2 kHz for high-throughput screening.[42] It requires the frame rate ($1/t$, where t is the exposure time) of optical detectors to be accordingly increased to resolve each individual droplet (Fig. 3c). The maximum measurable droplet frequency (*max. frequency* in Fig. 3c) is limited by the frame rate of the high-speed camera set during a measurement due to the fact that the exposure time should be shorter than the time interval between two consecutively passing droplets so as to avoid interference. The maximum frame rate of the camera which can be used for a measurement is further limited by the fluorescence intensity which drops drastically with the increase of the frame rate (Fig. 3c, black). Based on the level of the optical background as indicated in Fig. 3c, the maximum measurable droplet frequency with the optical decoding method is thus about 0.5 kHz. With respect to the magnetic measurement, the amplitude of magnetic voltage signals is constant with the increase of the sampling rate of the data acquisition box (DAQ) (Fig. 3c, red). Magnetic detection provides more reproducible results which are less sensitive to the flow speed that can be easily varied under different flow conditions in microfluidics. The maximum measurable droplet frequency with the magnetic decoding method for $N_d = 10$ as shown in Fig. 3c. Here N_d is the number of data points used to resolve a detection peak. The maximum measurable droplet frequency with magnetic detection is determined by the sampling rate of the DAQ and the number of data points used to resolve the signals, which is ~$1/N_d$ of the sampling rate of the DAQ. It applies to the case when droplets are produced in a *squeezing* regime that completely fills the cross-section of a microfluidic channel. In the present demonstration of droplet barcoding, the frequency of droplet detection is ~10 droplets per second (Fig. 2g). The frequency of detection can be increased by increasing the flow rates of oil and magnetic nanoparticles to increase the frequency of droplet formation and passing them across the sensor. With high flow rates, the droplet formation is governed by a *dripping* mechanism (Fig. 3f). For instance, when the flow rate of oil is increased from 30 nl s^{-1} to 900 nl s^{-1} and the flow rate of magnetic nanoparticles is increased from 10 nl s^{-1} to 100 nl s^{-1}, the size of droplets is reduced from 150 μm to 80 μm with a frequency of detection of ~240 droplets per second (Fig. 3d). The signal amplitude decreases with further reduction of the size of droplets due to the decrease in the amount of encapsulated magnetic nanoparticles. Further increasing the flow rate of oil to 1300 nl s^{-1} reduces the size of the produced droplets to about 60 μm, which is the minimum detectable size of droplets of this platform (Fig. 3e). As distinct signal levels should be created to encode droplets, the present platform should be operated for droplets with sizes larger than 100 μm to have the optimum encoding capability. To encode droplets smaller than 100 μm, the dimensions of the channel and the size of the GMR sensor should be reduced to produce smaller sizes of droplets and to enhance the sensitivity of measurements. Therefore, the further increase of the throughput of the detection can be relied on a prior collection of a large number of encoded droplets followed by reinjecting them for detection at high frequencies, which will not change the size of the produced droplets as in the case of the *dripping* regime.

Conclusions

We have presented a droplet-based magnetofluidic platform based on integrated GMR sensors which is composed of multiple functional areas to perform multiple tasks for droplet-based magnetic barcoding and decoding. The strategy of incorporating magnetic nanoparticles as joint barcodes into a conventional optical encoding scheme to increase the encoding capacity has been shown in this work. As a demonstration, the measured signals of magnetic and fluorescent encoded droplets can be used to identify the droplets carrying various concentrations of fluorescently modified penicillin. With this platform, two-dimensional joint barcodes comprising magnetic and optical codes can be easily prepared by the coencapsulation process. The incorporation of magnetic barcodes extends the encoding capacity by more than 1 order of magnitude compared with using solely optical codes.

The present barcoding platform demonstrates the feasibility of using such a magnetoresistive measurement approach as a potential decoding alternative to optical systems, paving the way for the development of novel non-optical encoding strategies for future droplet-based biological assays, such as combinatorial chemistry[50] where light-sensitive biomolecules

are involved. The use of the present platform could be of special importance in the field of synthesis chemistry, where light-sensible nanostructures (*i.e.* nanoparticles) could be negatively affecting the final products. Such barcoding system could be perceived as a potential platform to develop biological assays so as to avoid the use of optical labels, which can affect different cellular functions related to photocytotoxicity effects[51] or alter single cell mechanisms.[52,53] Moreover, magnetoresistance measurements offer the possibility of directly decoding (detection) real samples (*e.g.* human plasma, blood, and turbid fluids) as they are not affected by matrix interferences. Additionally, the use of magnetic codes needs only one decoding device (in this case, the GMR sensor), which can be easily integrated in any kind of platform, while for optical detection, the decoding process needs more fluorescence detectors with filters for each used label, making the measurement bulky and expensive.

However, several aspects can still be developed for magnetic barcodes for droplet microfluidics. The present coding is based on the intensity encoding mode, *i.e.*, different fluorescence or magnetic signal levels associated with different concentrations of fluorescent dyes or MNPs. To have a multiplexed droplet barcoding with an increased number of barcodes, the preparation of position-indexed magnetic barcodes that can be decoded with GMR sensors to display distinct detection peak patterns will be the next development step. The present platform provides a unique magnetic functional element for droplet microfluidics. Performing biological screening, combinatorial analyses and synthesis with droplet microfluidic platforms requires synergetic developments of multiple functional elements on-chip such as modules for droplet incubation, merging, dispensing and sorting, which are still an open issue and one of the major tasks for future development of droplet microfluidic platforms.

Acknowledgements

The authors thank C. Pahlke, L. Römhildt, and Dr. B. Ibarlucea (TU Dresden) as well as Dr. N. Pérez (IFW Dresden) for fruitful discussion, I. Fiering (IFW Dresden) for assistance in metal deposition and S. Harazim (IFW Dresden) for clean room support. We acknowledge financial support from the DFG Research Group 1713 and the European Research Council under the European Union's Seventh Framework Programme (FP7/2007-2013)/ERC grant agreement no. 306277.

Notes and references

1 L. Mazutis, J. Gilbert, W. L. Ung, D. A. Weitz, A. D. Griffiths and J. A. Heyman, *Nat. Protoc.*, 2013, **8**, 870–891.
2 S.-Y. Teh, R. Lin, L.-H. Hung and A. P. Lee, *Lab Chip*, 2008, **8**, 198–220.
3 A. B. Theberge, F. Courtois, Y. Schaerli, M. Fischlechner, C. Abell, F. Hollfelder and W. T. S. Huck, *Angew. Chem., Int. Ed.*, 2010, **49**, 5846–5868.
4 A. R. Abate, T. Hung, R. A. Sperling, P. Mary, A. Rotem, J. J. Agresti, M. A. Weiner and D. A. Weitz, *Lab Chip*, 2013, **13**, 4864–4869.
5 A. L. Markey, S. Mohr and P. J. R. Day, *Methods*, 2010, **50**, 277–281.
6 L. Baraban, F. Bertholle, M. L. M. Salverda, N. Bremond, P. Panizza, J. Baudry, J. A. G. M. de Visser and J. Bibette, *Lab Chip*, 2011, **11**, 4057–4062.
7 J. J. Agresti, E. Antipov, A. R. Abate, K. Ahn, A. C. Rowat, J.-C. Baret, M. Marquez, A. M. Klibanov, A. D. Griffiths and D. A. Weitz, *Proc. Natl. Acad. Sci. U. S. A.*, 2010, **107**, 4004–4009.
8 E. Brouzes, M. Medkova, N. Savenelli, D. Marran, M. Twardowski, J. B. Hutchison, J. M. Rothberg, D. R. Link, N. Perrimon and M. L. Samuels, *Proc. Natl. Acad. Sci. U. S. A.*, 2009, **106**, 14195–14200.
9 T. Schneider, J. Kreutz and D. T. Chiu, *Anal. Chem.*, 2013, **85**, 3476–3482.
10 K. Churski, T. S. Kaminski, S. Jakiela, W. Kamysz, W. Baranska-Rybak, D. B. Weibel and P. Garstecki, *Lab Chip*, 2012, **12**, 1629–1637.
11 M. T. Guo, A. Rotem, J. A. Heyman and D. A. Weitz, *Lab Chip*, 2012, **12**, 2146–2155.
12 W. Wang, J. R. Walker, X. Wang, M. S. Tremblay, J. W. Lee, X. Wu and P. G. Schultz, *Proc. Natl. Acad. Sci. U. S. A.*, 2009, **106**, 1427–1432.
13 S. R. Nicewarner-Pena, R. G. Freeman, B. D. Reiss, L. He, D. J. Pena, I. D. Walton, R. Cromer, C. D. Keating and M. J. Natan, *Science*, 2001, **294**, 137–141.
14 F. Cunin, T. A. Schmedake, J. R. Link, Y. Y. Li, J. Koh, S. N. Bhatia and M. J. Sailor, *Nat. Mater.*, 2002, **1**, 39–41.
15 H. Kim, J. Ge, J. Kim, S. Choi, H. Lee, H. Lee, W. Park, Y. Yin and S. Kwon, *Nat. Photonics*, 2009, **3**, 534–540.
16 R. J. Fulton, R. L. McDade, P. L. Smith, L. J. Kienker and J. R. J. Kettman, *Clin. Chem.*, 1997, **43**, 1749–1756.
17 H. Fenniri, L. Ding, A. E. Ribbe and Y. Zyrianov, *J. Am. Chem. Soc.*, 2001, **123**, 8151–8152.
18 M. Han, X. Gao, J. Z. Su and S. Nie, *Nat. Biotechnol.*, 2001, **19**, 631–635.
19 Z. Wang, S. Zong, W. Li, C. Wang, S. Xu, H. Chen and Y. Cui, *J. Am. Chem. Soc.*, 2012, **134**, 2993–3000.
20 Y. Zhao, Z. Xie, H. Gu, L. Jin, X. Zhao, B. Wang and Z. Gu, *NPG Asia Mater.*, 2012, **4**, e25.
21 X.-H. Ji, W. Cheng, F. Guo, W. Liu, S.-S. Guo, Z.-K. He and X.-Z. Zhao, *Lab Chip*, 2011, **11**, 2561–2568.
22 Y. Zhao, H. C. Shum, H. Chen, L. L. A. Adams, Z. Gu and D. A. Weitz, *J. Am. Chem. Soc.*, 2011, **133**, 8790–8793.
23 Y. Ding, S. Stavrakis, X. Casadevall i Solvas and A. J. deMello. *MicroTAS, the 17th International Conference on Miniaturized Systems for Chemistry and Life Sciences*, Freiburg, Germany, 2013, p. 299.
24 H. Xu, *Nucleic Acids Res.*, 2003, **31**, 43e–43.
25 C.-G. Yang, Z.-R. Xu, A. P. Lee and J.-H. Wang, *Lab Chip*, 2013, **13**, 2815–2820.
26 S. F. Medeiros, A. M. Santos, H. Fessi and A. Elaissari, *Int. J. Pharm.*, 2011, **403**, 139–161.

27 R. S. Gaster, D. A. Hall and S. X. Wang, *Lab Chip*, 2011, **11**, 950–956.
28 R. S. Gaster, D. A. Hall, C. H. Nielsen, S. J. Osterfeld, H. Yu, K. E. Mach, R. J. Wilson, B. Murmann, J. C. Liao, S. S. Gambhir and S. X. Wang, *Nat. Med.*, 2009, **15**, 1327–1332.
29 Y. R. Chemla, H. L. Grossman, Y. Poon, R. McDermott, R. Stevens, M. D. Alper and J. Clarke, *Proc. Natl. Acad. Sci. U. S. A.*, 2000, **97**, 14268–14272.
30 J. Loureiro, P. Z. Andrade, S. Cardoso, C. L. da Silva, J. M. Cabral and P. P. Freitas, *Lab Chip*, 2011, **11**, 2255–2261.
31 M. Helou, M. Reisbeck, S. F. Tedde, L. Richter, L. Bär, J. J. Bosch, R. H. Stauber, E. Quandt and O. Hayden, *Lab Chip*, 2013, **13**, 1035–1038.
32 E. J. Smith, W. Xi, D. Makarov, I. Mönch, S. Harazim, V. A. Bolaños Quiñones, C. K. Schmidt, Y. Mei, S. Sanchez and O. G. Schmidt, *Lab Chip*, 2012, **12**, 1917–1931.
33 D. Issadore, J. Chung, H. Shao, M. Liong, A. A. Ghazani, C. M. Castro, R. Weissleder and H. Lee, *Sci. Transl. Med.*, 2012, **4**, 141ra92.
34 I. Mönch, D. Makarov, R. Koseva, L. Baraban, D. Karnaushenko, C. Kaiser, K.-F. Arndt and O. G. Schmidt, *ACS Nano*, 2011, **5**, 7436–7442.
35 G. Lin, L. Baraban, L. Han, D. Karnaushenko, D. Makarov, G. Cuniberti and O. G. Schmidt, *Sci. Rep.*, 2013, **3**, 2548.
36 S. J. Osterfeld, H. Yu, R. S. Gaster, S. Caramuta, L. Xu, S.-J. Han, D. A. Hall, R. J. Wilson, S. Sun, R. L. White, R. W. Davis, N. Pourmand and S. X. Wang, *Proc. Natl. Acad. Sci. U. S. A.*, 2008, **105**, 20637–20640.
37 N. Pekas, M. D. Porter, M. Tondra, A. Popple and A. Jander, *Appl. Phys. Lett.*, 2004, **85**, 4783.
38 D. Nathwani and M. J. Wood, *Drugs*, 1993, **45**, 866–894.
39 Y. Horiuchi and K. Shibata, *Int. Arch. Allergy Appl. Immunol.*, 1965, **28**, 306–320.
40 M. N. Baibich, J. M. Broto, A. Fert, F. N. Van Dau and F. Petroff, *Phys. Rev. Lett.*, 1988, **61**, 2472–2475.
41 G. Lin, D. Makarov, M. Melzer, W. Si, C. Yan and O. G. Schmidt, *Lab Chip*, 2014, **40**, 4050–4058.
42 J.-C. Baret, O. J. Miller, V. Taly, M. Ryckelynck, A. El-Harrak, L. Frenz, C. Rick, M. L. Samuels, J. B. Hutchison, J. J. Agresti, D. R. Link, D. A. Weitz and A. D. Griffiths, *Lab Chip*, 2009, **9**, 1850–1858.
43 N.-T. Nguyen, *Microfluid. Nanofluid.*, 2011, **12**, 1–16.
44 I. Jeong, Y.-J. Eu, K. W. Kim, X. Hu, B. Sinha and C. Kim, *J. Magn.*, 2012, **17**, 302–307.
45 E. Kurtoğlu, A. Bilgin, M. Şeşen, B. Mısırlıoğlu, M. Yıldız, H. F. Y. Acar and A. Koşar, *Microfluid. Nanofluid.*, 2012, **13**, 683–694.
46 N.-T. Nguyen, A. Beyzavi, K. M. Ng and X. Huang, *Microfluid. Nanofluid.*, 2007, **3**, 571–579.
47 J. S. Sander, R. M. Erb, C. Denier and A. R. Studart, *Adv. Mater.*, 2012, **24**, 2582–2587.
48 S. K. Suh, S. C. Chapin, T. A. Hatton and P. S. Doyle, *Microfluid. Nanofluid.*, 2012, **13**, 665–674.
49 P. Garstecki, M. J. Fuerstman, H. A. Stone and G. M. Whitesides, *Lab Chip*, 2006, **6**, 437–446.
50 C. Carbonell, K. C. Stylianou, J. Hernando, E. Evangelio, S. A. Barnett, S. Nettikadan, I. Imaz and D. Maspoch, *Nat. Commun.*, 2013, **4**, 2173.
51 S. Banerjee, P. Prasad, A. Hussain, I. Khan, P. Kondaiah and A. R. Chakravarty, *Chem. Commun.*, 2012, **48**, 7702–7704.
52 V. Lulevich, Y.-P. Shih, S. H. Lo and G.-Y. Liu, *J. Phys. Chem. B*, 2009, **113**, 6511–6519.
53 F. Progatzky, M. J. Dallman and C. Lo Celso, *Interface Focus*, 2013, **3**, 20130001.
54 A. Fedarovich, K. A. Djordjevic, S. M. Swanson, Y. K. Peterson, R. A. Nicholas and C. Davies, *PLoS One*, 2012, **7**, e44918.
55 J. Ayala, A. Quesada, S. Vadillo, J. Criado and S. Píriz, *J. Med. Microbiol.*, 2005, **54**, 1055–1064.
56 G. Zhao, T. I. Meier, S. D. Kahl, K. R. Gee and L. C. Blaszczak, *Antimicrob. Agents Chemother.*, 1999, **43**, 1124–1128.
57 W. Hu, R. J. Wilson, A. Koh, A. Fu, A. Z. Faranesh, C. M. Earhart, S. J. Osterfeld, S.-J. Han, L. Xu, S. Guccione, R. Sinclair and S. X. Wang, *Adv. Mater.*, 2008, **20**, 1479–1483.

